International Journal of Remote Sensing

Mapping of the 26 December 2004 tsunami disaster by using FORMOSAT-2 images

PLEASE SCROLL DOWN FOR ARTICLE

Taylor & Francis
Taylor & Francis Group

Mapping of the 26 December 2004 tsunami disaster by using FORMOSAT-2 images

M. D. YANG*†, T. C. SU†, C. H. HSU†, K. C. CHANG‡ and A. M. WU§

†Department of Civil Engineering, National ChungHsing University, Taichung, Taiwan
‡Department of Geography, National Taiwan Normal University, Taipei, Taiwan
§Division of Systems Engineering, National Space Organization, Hsinchu, Taiwan

The Sumatra earthquake struck South Asia on 26 December 2004 and triggered monstrous waves that turned into a tsunami hitting the ocean regions and caused the most severe natural disaster of recent decades. The devastating earthquake and tsunami changed the landscape of coastal areas in many countries around the whole Indian Ocean region. To provide real-time information for rescue and rehabilitation plans, satellite images were applied to monitor and evaluate the damage over several devastated spots. The FORMOSAT-2 satellite, which was launched on 21 May 2004 and operated by the National Space Organization, Taiwan, is uniquely designed to take timely and low-cost black and white images daily with a resolution of 2 m and colour images of 8-m resolution. FORMOSAT-2 is expected to have many useful applications, such as natural-disaster evaluation, land-usage analysis, environmental monitoring, and coastal search and rescue. FORMOSAT-2 successfully acquired several post-tsunami images of the hazardous areas, both Puhket, Thailand and Banda Aceh, Indonesia on 28 December. A series of FORMOSAT-2 satellite images were processed by geometric and radiometric correction, haze reduction, image enhancement, feature extraction, image classification, and image fusion to assess the damage over those devastated areas. FORMOSAT-2 satellite images with a high-temporal resolution and high-spatial resolution were proved to be an efficient and useful information source for decision-makers to make rescue and recovery plans, especially for some isolated islands hard to reach in time.

1. Introduction

Natural hazards are considered to be a destined disaster, but limited prevention and reduction approaches can be adopted due to a great deal of coordination. Efficient disaster mitigation and rescue action relies on timely and effective information on hazard areas. Unfortunately, natural hazards are often widespread, and the devastated areas are sometimes unreachable so that an overall *in situ* investigation becomes difficult or impossible. As a rapid technology development in space platform and digital imagery, remote-sensing data have been broadly applied to Earth surface monitoring in recent decades, such as agriculture monitoring (Rydberg and Borgefors 2001, Murthy *et al.* 2003), environmental change (Piwowar *et al.* 1998), as well as water-pollution assessment (Yang *et al.* 1999, Cheng and Lei 2001, Chen 2003). With regard to applying remote sensing to natural-hazard investigation and management, several studies have been reviewed.

---

*Corresponding author. Email: mdyang@dragon.nchu.edu.tw

Landsat5 TM images were applied to identify the neotectonic features of the 7 September 1999 Athens earthquake (Ganas *et al.* 2001). Gupta and Joshi (1990) and Lin *et al.* (2000, 2002) used remote sensing and Geographic Information System (GIS) techniques in assessing landslides and debris flows. The US National Oceanic and Atmospheric Administration monitors droughts on large areas by developing an Advanced Very High Resolution Radiometer (AVHRR)-based Vegetation Condition Index (VCI) derived from a Normalized Difference Vegetation Index (NDVI) and Temperature Condition Index (TCI) derived from AVHRR-measured radiances (Kogan 1997). SPOT satellite images were used to analyse NDVI for comparison and evaluation of the vegetation recovery rates before and after the Chi-Chi Earthquake (Lin *et al.* 2004a). Aerial photographs and SPOT satellite images were coupled to assess the damage level and potential risk of collapsed spots on the Tsao-Ling landslide caused by the Chi-Chi Earthquake (Yang *et al.* 2004). A synthetic probability map of the Tsao-Ling landslide reoccurrence was produced that provided efficient information for planning an emergency response and developing a rehabilitation strategy. Also, automated classifications were developed and applied to SPOT satellite images for the recognition of landslide hazards (Yang and Yang 2004, Yang *et al.* 2005). The integration of GIS, remote sensing, and GPS can provide a low-cost and rapid methodology for disaster management as well as critical information for decision support using emergency managers and the disaster-response community (Montoya 2003, Tralli *et al.* 2005). A decision-support system (DSS) for open mining areas during the formulation of a restoration plan was developed using thematic maps derived from Earth observation data (Ganas *et al.* 2004).

Satellite images provide several advantages in hazard monitoring, such as digital data, large area coverage, and the ability to perform routine, repetitive, continuous, and economical image acquisition. Compared with aerial photography, however, satellite images have a lower spatial resolution, which limits their applications in urban areas. With the launch of IKONOS-1 in 1999 and QUICKBIRD in 2001, a new era of a commercial satellite image with a high spatial resolution has begun by offering panchromatic images with a resolution of 1 m and 0.6 m as well as 4-m and 2.44-m multispectral images, respectively. The land-cover map derived from IKONOS satellite images was used as input for the flood simulation model, LISFLOOD-FP, to produce a Manning roughness factor map for the inundated areas (Van Der Sande *et al.* 2003). Intensity–Hue–Saturation (IHS) was used to integrate hyperspectral and radar data into a single image of an urban area by image fusion that provided rich information necessary for assessment and mitigation of hazards in urban-disaster management (Chen *et al.* 2003). High-resolution digital-elevation models (e.g. from InSAR, Lidar, and digital photogrammetry) and image spectroscopy (e.g. using ASTER, MODIS, and Hyperion) are believed to contribute significantly to hazard management of natural disasters, such as earthquakes, volcanoes, floods, landslides, and coastal inundation (Tralli *et al.* 2005).

However, high-spatial-resolution images do not meet the demands of a complete disaster management. A better temporal resolution (revisit capability) is desirable during the hazard response and recovery due to their emphasis on 'real-time' information about a disaster area. In this paper, a new civilian satellite with both high spatial and temporal resolutions, FORMOSAT-2, was employed for remote monitoring of the severe nature disaster from the earthquake- and tsunami-devastated areas of the Sumatra catastrophe. FORMOSAT-2 offers images

with a high spatial resolution of 2-m panchromatic and 8-m multispectral as well as a high temporal resolution of 1 day. Thus, FORMOSAT-2's superior temporal frequency of remote-sensing data acquisitions means that satellite images could be used in disaster-management response and recovery.

2. Hazard monitoring using satellite images

Hazard management involves four phases in a cycle which should consist of mitigation, preparedness, response, and recovery (Montoya 2003). Remote sensing has been playing a key role in disaster-mitigation activities, including risk assessment and reducing potential effects of disasters. The spatial and temporal anomalies of the Earth's emitted radiation in the thermal infrared spectral range (TIR) measured from satellites have been analysed for monitoring seismically active regions (Tramutoli *et al.* 2005). Geospatial information products derived from remote-sensing data address the operational requirements of hazard decision-support systems, which is helpful in risk assessment, mitigation planning, disaster assessment, and response prioritization for policymakers, emergency managers, and responders (Tralli *et al.* 2005). Various useful information, such as land use, land cover, infrastructures, human settlements, topography, vegetation recovery index, morphology and geology for risk analysis, and hazard maps can be extracted from remote-sensing data (Rivereau 1995, Van Der Sande *et al.* 2003, Lin *et al.* 2004a and 2004b, Yang *et al.* 2004, Tralli *et al.* 2005). Preparedness involves planning actions in a disaster and trying to increase the available rescue resources. The information for risk analysis extracted from high-spatial-resolution satellite imagery can be introduced into GIS to establish a disaster-relief database for preparedness (Rivereau 1995). Response relates to all possible emergency activities immediately following a disaster occurrence. When a disaster has taken place, short-term and long-term recovery continues until all life-support systems are back to normal (Montoya 2003). The recovery rate of an ecosystem can be successfully estimated by comparing satellite images before and after the disaster (Lin *et al.* 2004a).

Among these four phases of hazard management, satellite imagery provides limited support during the short period of the disaster response due to its deficient temporal resolution for instant reactions immediately following a disaster. Response emphasizes 'real time'; therefore, temporal efficient data extracted from satellite images need to be acquired in a very short period of time. Timely data derived from high-temporal-resolution satellite imagery can be acquired to assess damage extent rapidly after a disaster, although some natural hazards do not enable cloud-free images to be obtained (Rivereau 1995). However, the response phase is the most critical portion of the disaster cycle because of its providing emergency assistance to victims of an event and reducing the likelihood of secondary damage. Thus, routine, repetitive, and continuous observations of the Earth's surface from high-temporal-resolution satellite imagery is very useful for acquiring rapid assessment in order to take immediate and effective action in the disaster response phase (Piwowar *et al.* 1998, Montoya 2003). The application of satellite images to a disaster response includes several steps, including orbit determination, image acquisition, data preparation, image processing, image interpretation, and decision support for a disaster response. Through the analysis process, high-temporal-resolution satellite imagery can assist authorities in making disaster-response decisions and further recovery plans. In the recovery phase. routine, repetitive, and continuous observations of the Earth's surface from operational satellites with high-temporal-resolution imagery

are useful in assessing hazard impacts and making recovery plans (Piwowar *et al.* 1998, Montoya 2003). Also, satellite images are suitable for a long-term assessment of environment and ecosystem recovery.

3. FORMOSAT-2 brief

Like other developed countries, Taiwan is facing dynamic changes in land use due to rapid economic growth and frequent natural disasters such as earthquakes and typhoons. In the aftermath of a disaster, there is an urgent need for timely remote-sensing data to monitor and assess damage. Thus, in 1991, the National Space Organization (NSPO) was founded by the National Science Council (NSC) as a governmental agency to execute the national space program (NSPO 2005). Currently, two satellites are operated by NSPO to collect remote-sensing data. The first NSPO satellite, FORMOSAT-1, was successfully launched in 1999 to carry out three scientific research missions, including ocean colour imaging, experiments on ionospheric plasma and electrodynamics, and Ka-band (20–30 GHz) communications experiments. The second satellite, FORMOSAT-2, takes land images to meet Taiwanese civilian needs by providing black and white images with a resolution of 2 m and colour images of 8-m resolution (table 1). Also, an imager on board FORMOSAT-2 observes upper atmospheric lightning (the first time from a satellite).

FORMOSAT-2, formerly known as ROCSAT-2, was successfully launched on 21 May 2004 (Taipei Time) and acquired the first image at 9.39 a.m. on 4 June (Wu and Wu 2004). To provide timely and low-cost image data, FORMOSAT-2 can daily monitor the environment and resources throughout the Taiwan main island, offshore remote islands, the Taiwan Strait, the surrounding ocean, and other regions under international cooperation. FORMOSAT-2 is expected to have many useful applications, such as agriculture and forestry prediction, natural-disaster evaluation, land-usage analysis, environmental monitoring, coastal search and rescue, academic research, and extension education. Especially for natural-disaster evaluation, FORMOSAT-2 images are very valuable for assessing damage using tasking orders possibly within a day if weather allows. The conditions of flood-submerged fields, landslides, debris flows, and the structural integrity of hillsides can be assessed. A couple of significant contributions by FORMOSAT-2 in monitoring and evaluating

Table 1. FORMOSAT-2 remote-sensing instrument specification.

Payload	Remote Sensing Instrument (RSI)
	Imager of Sprites and Upper Atmospheric Lightning (ISUAL)
Weight	742 kg (with payload and fuel)
Shape	Hexahedron, height 2.4 m, outer diameter about 1.6 m
Orbit	891 km, sun-synchronous, two passes over Taiwan Strait each day
Panchromatic (PAN)	0.45~0.90 μm
Multi-spectrum (MS)	0.45~0.52 μm blue; 0.52~0.60 μm green
	0.63~0.69 μm red; 0.76~0.90 μm near-infrared
Ground sampling distance (GSD)	2 m for black and white images; 8 m for colour images
Swath	24 km
Mission life	5 years
Launch date	21 May 2004 (Taipei Time)

natural disasters in Taiwan include the flooding and debris flows brought by Typhoons Midully and Aere in summer 2004 (Chang *et al.* 2004, Lin *et al.* 2004b).

4. FORMOSAT-2 images of the South Asia catastrophe

The great South Asia earthquake (M_w 9.0) on 26 December 2004 generated a tsunami in the Indian Ocean, which struck the coastal regions of Sumatra, Thailand, Sri Lanka, and southern India. The earthquake was caused by the release of stresses accumulated as the Burma tectonic plate overrides the India tectonic plate (USGS 2005). Data from 60 Global Positioning Systems (GPS) in South East Asia were collected to identify the crustal deformation caused by the Sumatra earthquake (Vigny *et al.* 2005). Movement of the seafloor generated a tsunami, or seismic sea wave, due to the earthquake off Indonesia's Sumatra island. Over 170 000 people were reported dead or missing due to the tsunamis unleashed by the quake.

For an instant response to the natural disaster, catastrophic images were acquired in 2 days by an emergency orbit scheduling. Passing over South Asia on its second satellite orbit as shown in figure 1, FORMOSAT-2 is one of the first remote-sensing satellites to successfully take images of Phuket Island and Banda Aceh, two heavily hit areas, within 2 days after the disaster (table 2). These images were processed and provided to aid rescuers working in those areas through channels of the Department of Foreign Affairs and research centres of Taiwan. Meanwhile, FORMOSAT-2 continued imaging up to an additional month for those seriously hit areas including the west coast of Thailand, Sumatra of Indonesia, eastern coast of India, Sri Lanka, Andaman, and Nicobar Islands. Highly efficient data propagation increases the benefits by remote-sensing data sharing and dissemination, and so NSPO established a window of opportunity through the Internet for public access to the
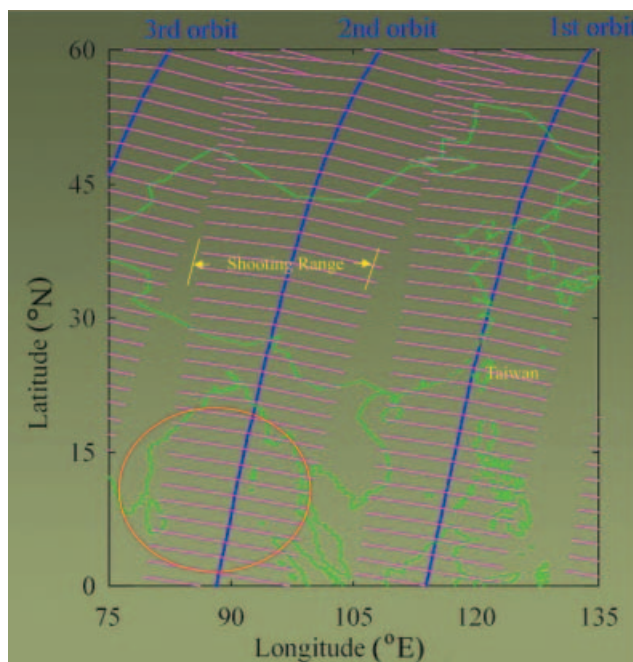

Figure 1.   FORMOSAT-2 orbits covering Asia (circle representing the devastated area in the Sumatra catastrophe).

Table 2. Process timetable of FORMOSAT-2 imagery.

Sequence	Time needed (h)
Order	2
Scheduling	2
Imaging	2~24
Acquisition	2
Processing	2
Distribution	2
Total	12~34

FORMOSAT-2 image database. All available images listed in table 3 could be downloaded from the Internet at http://www.nspo.org.tw/tsunami_images for those affected countries free of charge for 2 months after the tsunami. Several images of devastated regions were analysed in this paper, as shown in figure 2.

A standard level-II product of FORMOSAT-2 had been adjusted through geometric and radiometric correction (Wu *et al.* 2003, Chen *et al.* 2004). Level-II FORMOSAT-2 images, such as south-western Thailand, Phuket Island, and Aceh province are shown in figures 3–5. For a better visual interpretation, fusion images were produced using a multiplicative algorithm on high-spatial-resolution 2-m panchromatic images and high-spectral-resolution 8-m multispectral images. The fusion images provide rich information necessary for hazard assessment and mitigation.

Furthermore, for hypertemporal image analysis, three requirements must be met: (1) univariate at each temporal image; (2) precise co-registration; and (3) radiometric consistency (Piwowar *et al.* 1998). Ground control points (GCPs) and local reference maps could facilitate advanced geo-rectification if necessary. Most of all, radiometric correction is the major process affecting the analysis of multiple-date satellite images. These multi-temporal images were radiometrically corrected by first using the Pseudoinvariant Feature (PIF) method to locate possible dark and bright objects (the same buildings, roads, and water pixels on both images) and then carrying out a radiometric control set (RCS) method on the selected pixels to determine the correlation coefficients between images for each band of the multi-spectral images (Yang and Lo 2000, Ya'allah and Saradjian 2005). Under the assumption that at least some pixels have the same average surface reflectance among images acquired at different dates, the RCS method examines the band-to-band scattergrams in which the pixels have little or no variation between the dates of image acquisition. The radiometric methods were employed to correct the digital numbers (DN) on the 31 December image based on the 28 December image for Phuket Island in this research. The radiometric rectification equations of the 31 December image were acquired by linear regression as follows:

$$DN_{band1'} = 1.2116 DN_{band1} - 26.873; \ R^2 = 0.917 \tag{1}$$

$$DN_{band2'} = 1.2165 DN_{band2} - 18.395; \ R^2 = 0.958 \tag{2}$$

$$DN_{band3'} = 1.1664 DN_{band3} - 8.5458; \ R^2 = 0.964 \tag{3}$$

$$DN_{band4'} = 1.2462 DN_{band4} - 17.781; \ R^2 = 0.972. \tag{4}$$

Table 3. List of available FORMOSAT-2 catastrophe images.

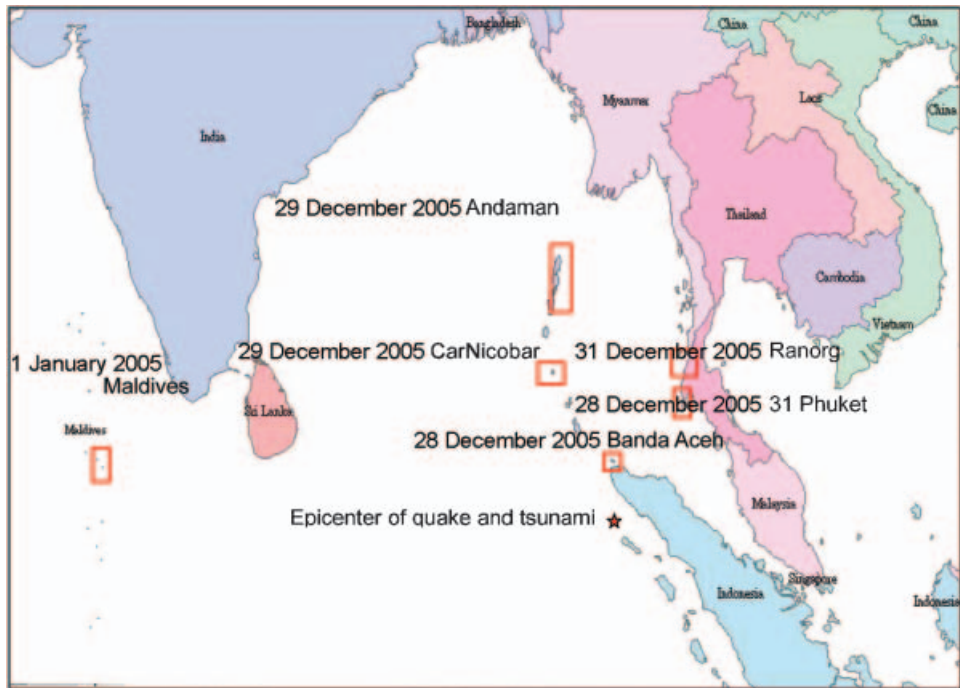| Location	Date	Frames
Anankwin	7 January 2005	2
Andaman	29 December 2004	4
	30 December 2004	4
Ban Na Kha	9 January 2005	2
Banda Aceh	28 December 2004	2
	4 January 2005	2
	8 January 2005	1
	10 January 2005	1
BandaAceh Indonesia	23 January 2005	2
Belingru	7 January 2005	2
Bokpyin	7 January 2005	2
	10 January 2005	2
Cadale	8 January 2005	2
Car Nicobar	29 December 2004	1
Daba Gallo	6 January 2005	2
Dabaro	7 January 2005	2
Dawei	31 December 2004	6
Dhuudo	9 January 2005	1
Garaced	8 January 2005	2
Karathuri	9 January 2005	2
Karen Taungbyauk	18 January 2005	2
Krabi	5 January 2005	2
Lammasingi	16 January 2005	2
Lammasingi India	13 January 2005	2
Lanbikyun	4 January 2005	2
Lawthaing	9 January 2005	2
Lawthaing Indonesia	23 January 2005	2
Leungah	18 January 2005	2
Lhokseumawe	5 January 2005	2
Lhokseumawe Indonesia	22 January 2005	2
	20 January 2005	2
Madras	13 January 2005	2
Maldive Islands	1 January 2005	3
Mergui	6 January 2005	2
Meulaboh	6 January 2005	2
Mudon	6 January 2005	2
Myinmoletkat	10 January 2005	2
Neman India	14 January 2005	2
Nooleeye	13 January 2005	2
Pasilho Indonesia	21 January 2005	2
Phuket	28 December 2004	4
	31 December 2004	8
Ranong	31 December 2004	6
	18 January 2005	2
Sigli	9 January 2005	1
Somalia	5 January 2005	2
Spitpyit	8 January 2005	2
Sri Lanka	13 January 2005	2
Tadepallegudem	14 January 2005	2
	16 January 2005	2
Takua	8 January 2005	2
Taungkhaya	8 January 2005	2
	15 January 2005	2
Trang	10 January 2005	2
Trincomalee	15 January 2005	1
Ujungblang Indonesia	20 January 2005	2

Figure 2. Rectangular marks illustrating the study areas damaged by the Sumatra earthquake and tsunami (asterisk representing its epicentre).

The high correlation coefficients of regression results show a significant confidence in terms of radiometric correction.

5. Image interpretation and analysis

After being corrected for geometry and post-processed, the FORMOSAT-2 image is suitable for constructing approximately 1 : 24 000 scale maps in true or false colour that can be analysed for monitoring the disaster damage. However, because of the lack of entire on-site information, such as GCPs, digital elevation model (DEM), and ground true reference, the interpretation and analysis of images was limited to fundamental analysis and interpretation. The extent and localization of the tsunami damages were analysed through either visual interpretation on the fusion images or digital analysis on multispectral FORMOSAT-2 images, including haze reduction, feature extraction, image classification, contrast enhancement, and band-ratio analysis on Erdas Imagine. To provide information promised to help cope with the tsunami catastrophe, several important discovery and analysis results were addressed in the subset images of interest, which are useful for disaster region positioning, damage-level assessment, rescue planning, and environmental-impact evaluation (figures 6–11).

The extent and localization of the damage were estimated by digital analysis of the differences between struck and non-struck areas. VI (vegetation index) and NDVI were analysed for revealing the extent of intruded area by the tsunami. Near-infrared (NIR) reflectance intensity is related most to vegetation condition and inversely to water content. Destroyed vegetation and high water content caused by the tsunami reduced NIR reflectance intensity in the inundated terrains. Immersed
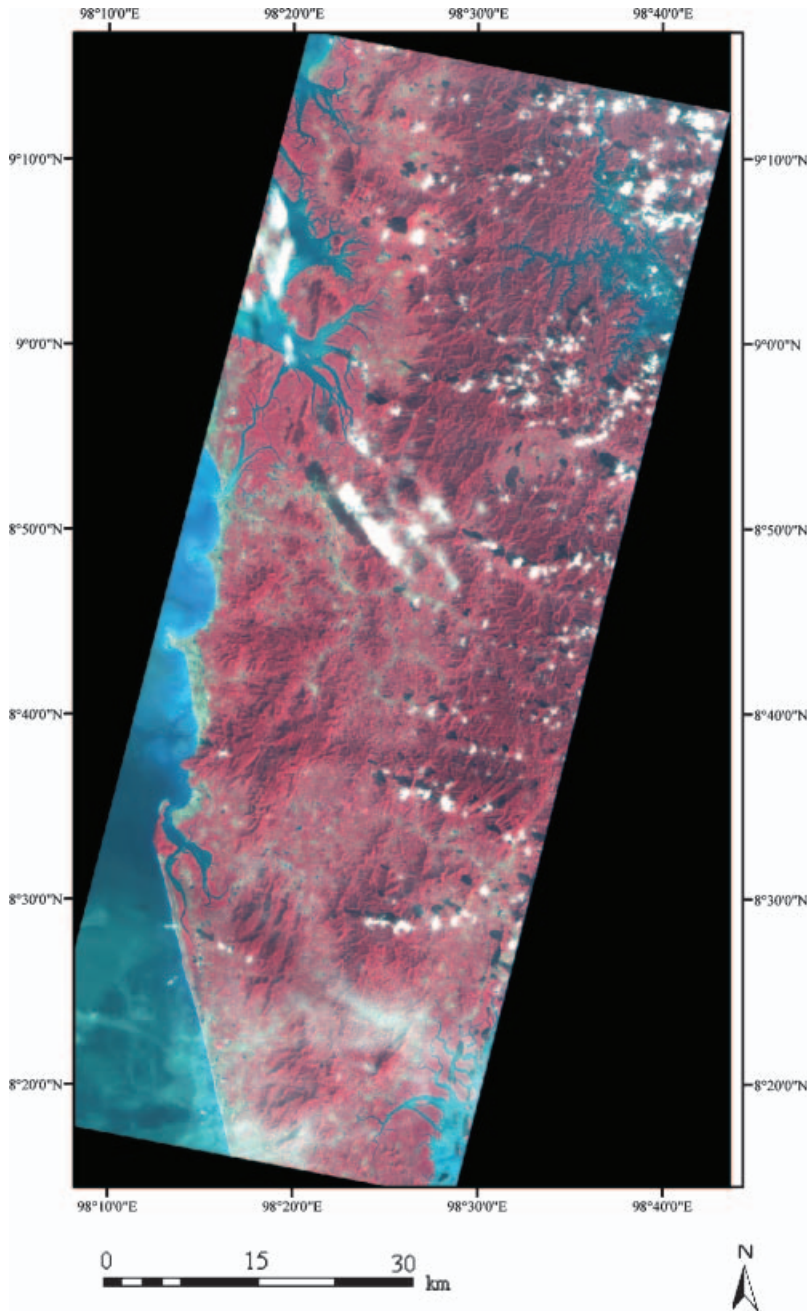
Figure 3. Fusion false-colour IR image of the south-western Thailand along the Andaman Sea taken on 31 December 2004 with a sun azimuth of 138.45°, sun elevation of 47.25°, viewing angle of 36.9978°, and incidence angle of 43.31°.

areas after the tsunami reflect a weaker NIR than do non-struck areas. Moreover, the scooped terrain by the tsunami flood wave increases red reflectance intensity. Thus, the VI or NDVI analysis is helpful for interpreting the boundary between the struck and non-struck areas.
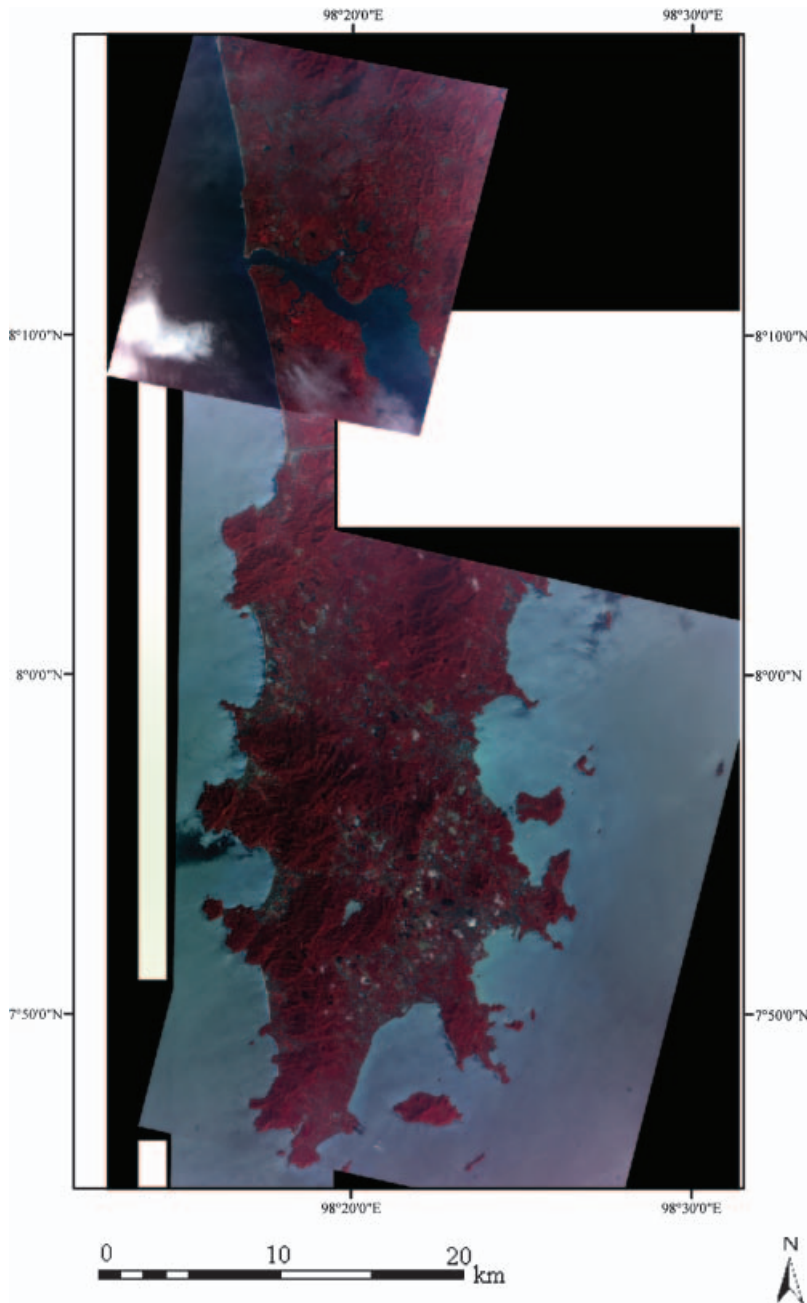
Figure 4.   Fusion false-colour IR image of Phuket Island, Thailand, which is a mosaic image consisting of FORMOSAT-2 images taken on 28 and 31 December 2004.

Figure 6 shows the destructions of Ranong, western Thailand, along the Andaman Sea. Figure 6(*a*1) shows false-colour NIR fusion imagery for Khao Lak revealing the destruction by the tsunami where is a portion of Khao Lak, Ram Lu National Park. The long-term impact upon the ecological environment must be paid attention in the future. Figure 6(*a*2) shows the NDVI analysis of original
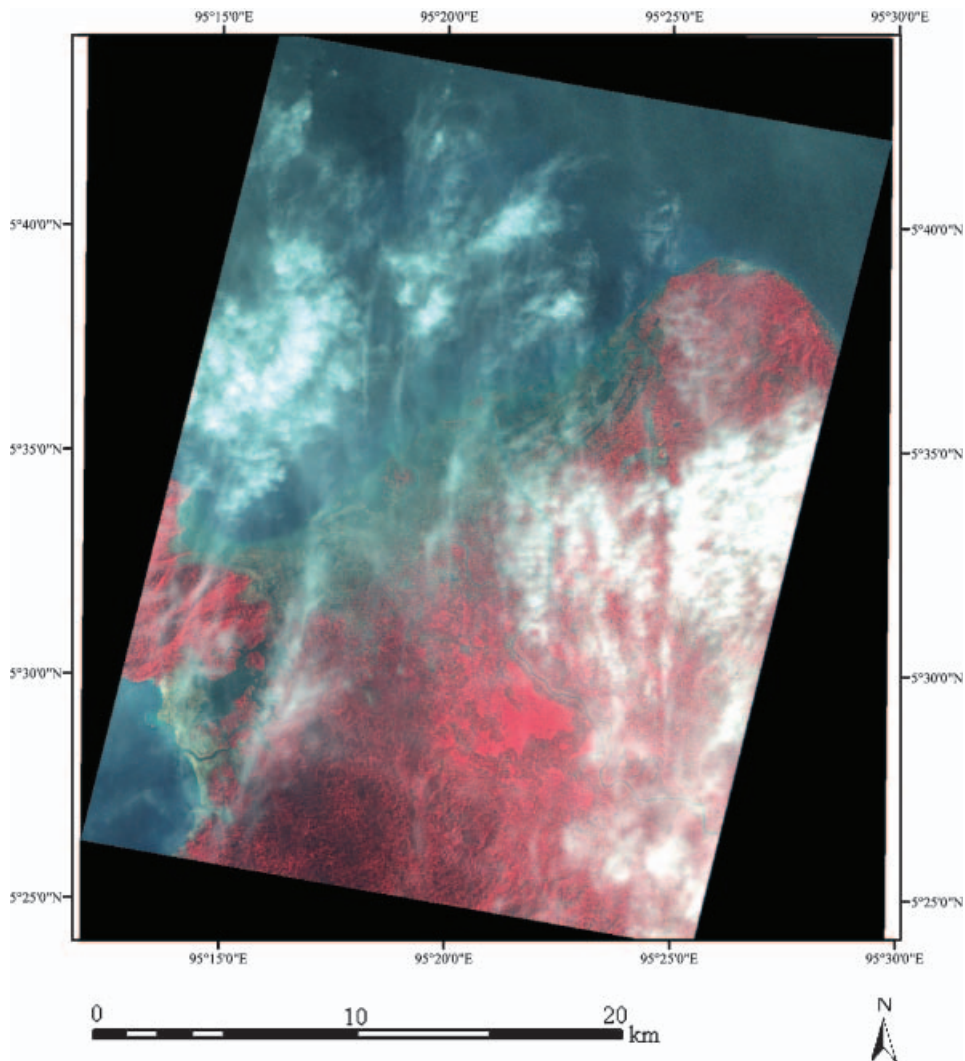
Figure 5. Fusion false-colour IR image of Banda Aceh, Indonesia taken on 28 December 2004 with a sun azimuth of 134.19°, sun elevation of 47.71°, viewing angle of 26.5501°, and incidence angle of 30.63°.

multi-spectral images. A distinguishable difference of NDVI values between the struck and non-struck areas along the coastline illustrates the extent of the tsunami inundation resulting in a negative NDVI value. Also, the indentation eroded by the tsunami in the coastline becomes more evident in the NDVI map. Figure 6(*b*) shows the overwhelmed wooden houses in the vacationland in Thap Lamu, Ranong. Mud and clay brought by the flood wave covered most of the vacationland so that the traffic network was interrupted. The entire village will need to be rebuilt.

With many hotels and golf clubs built in the neighbourhood of the beach area, Thailand's Phuket is a world-famous resort island and was devastated in this disaster. Traffic facilities such as roads, bridges, and airports, affect the efficiency of disaster relief. Important traffic infrastructures, such as the Sarasin Bridge connecting Phuket Island and mainland Thailand in figure 7(*a*) and the Phuket
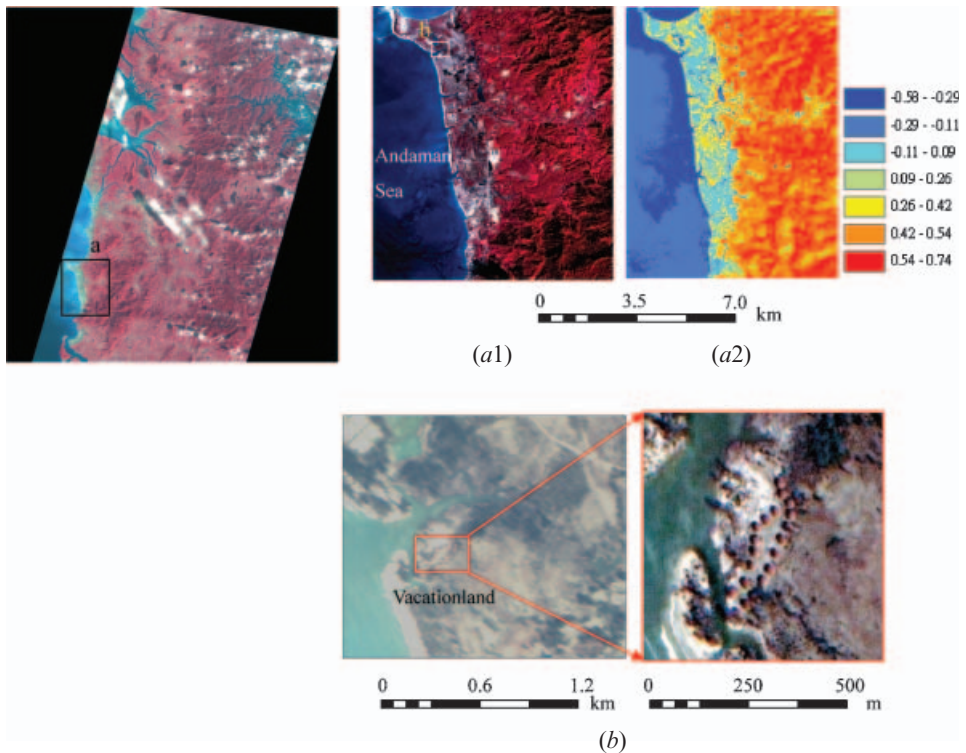
Figure 6.   Destruction of Ranong, western Thailand, along the Andaman Sea. (*a*1) Devastated area of Khao Lak. (*a*2) NDVI analysis, helpful for determining the extent of tsunami destruction. (*b*) Overwhelmed wooden houses in vacationland in Thap Lamu, Ranong.

International Airport for international aids in figure 7(*b*), were undamaged and could accommodate emergency rescue and recovery. An international airlift was still allowed to ferry critical aid and medicine to Phuket and also to take surviving travellers home. Figure 7(*c*1) shows that Bang Thao, one of the coastal towns in the western Phuket Island, had only minor destruction after the tsunami. The clinic and clubs were safe to provide medicine aid and disaster shelters. The main road, Scenic Coastal Drive, was not destroyed by the floodwaters. Moreover, to improve the visual appearance of waves, contrast enhancement was conducted on the extracted water body from the panchromatic imagery. Through a histogram analysis and linear stretch, the waterfront was magnified. In this recreation beach area, the wave condition usually is calm inside the fiord; the wavefront is parallel to, and the wave direction perpendicular to, the shoreline due to the dragging effect on the sea bed and coastal terrain. The unusual wave height and pattern in the Ban Thao beach indicate the attacking direction of the tsunami as red arrows in figure 7(*c*2). Figures 7(*d*1) and (*d*2) show false-colour NIR fusion images of Bang Khu in the eastern coast of Phuket taken on 28 and 31 December, respectively. Comparing these two radiometrically corrected images, we discovered that flooding vanished in the coast region and the submerged land reappeared on 31 December. Figure 7(*e*) shows fusion images of Patong, a famous international resort town, in true colour and NIR false colour. The west side of Patong by Rat U-Thit Songroi Pi Road, where there are many scenic spots and quality hotels, was drastically lashed by the
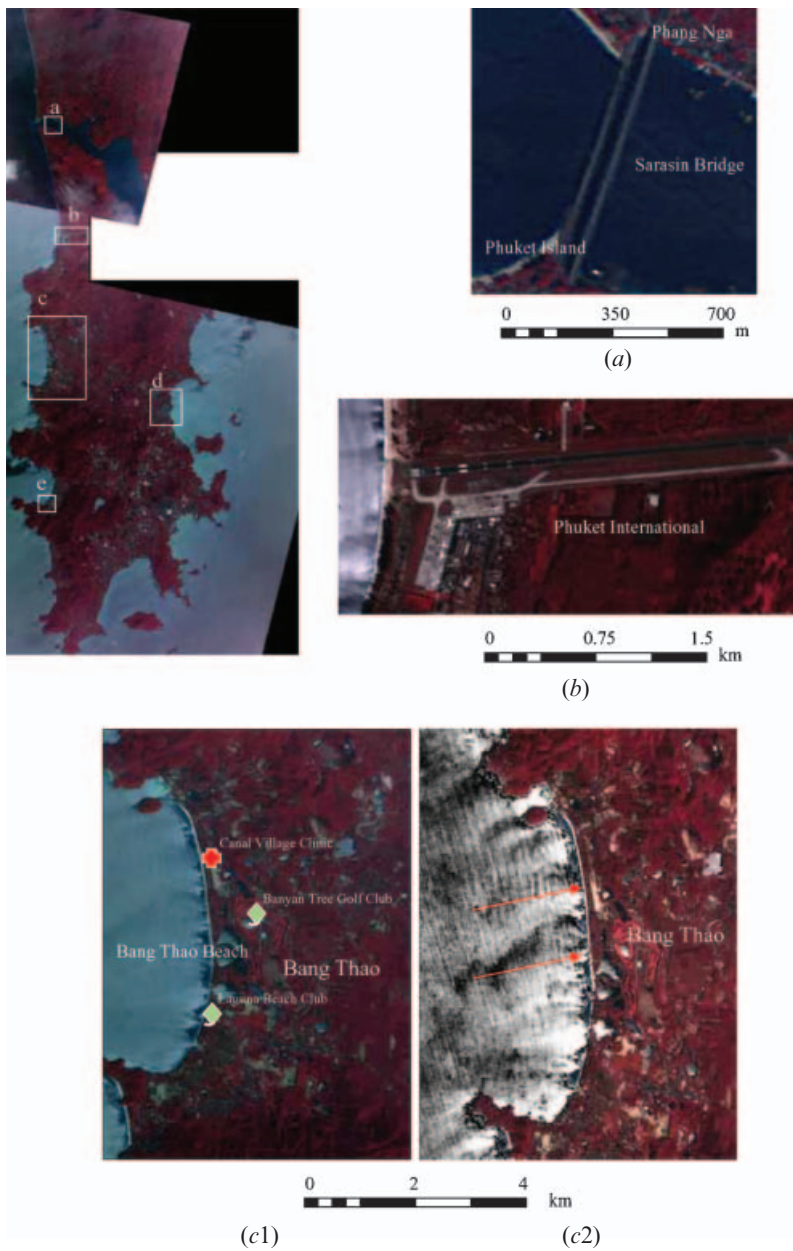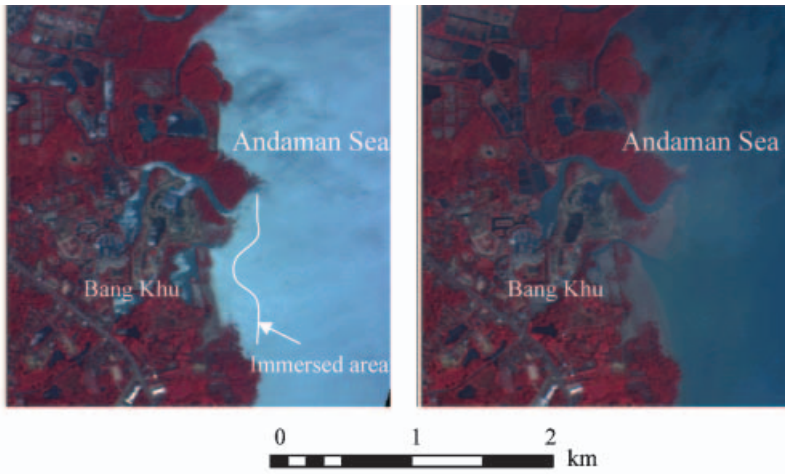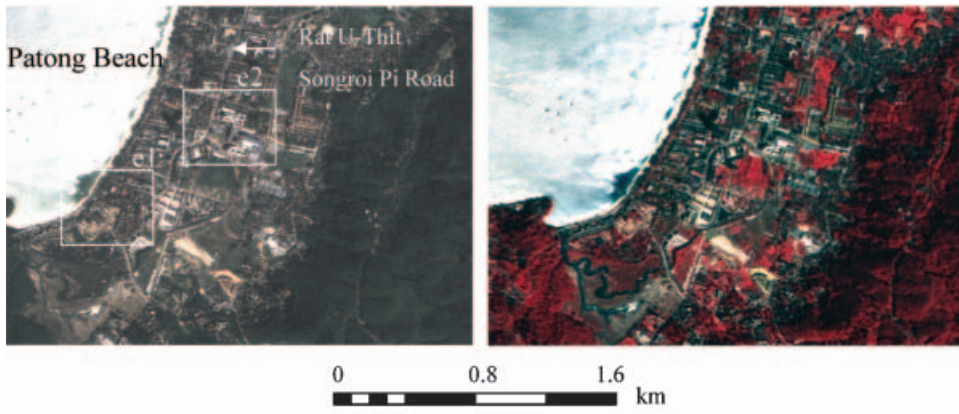
Figure 7. Post-tsunami Phuket island images. (*a*) Sarasin Bridge connecting Phuket Island and mainland Thailand. (*b*) Phuket International Airport for international aids. (*c*1) Bang Thao resort. (*c*2) Enhanced image with a magnified waterfront showing the attacking direction of the tsunami (red arrows). (*d*1) IR fusion image of Bang Khu on 28 December. (*d*2) IR fusion image of Bang Khu on 31 December. (*e*) Fusion images of Patong in true colour and IR false colour. (*e*1) Patong Merlin Clinic. (*e*2) Royal Paradise Clinic.
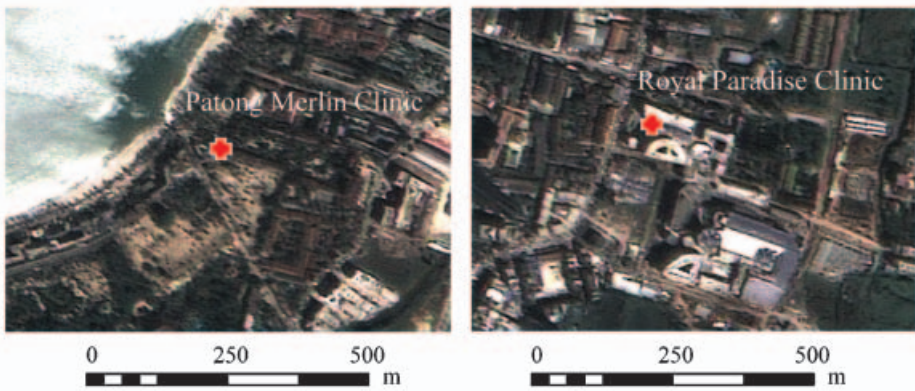
(*d*1) (*d*2)

(*e*)

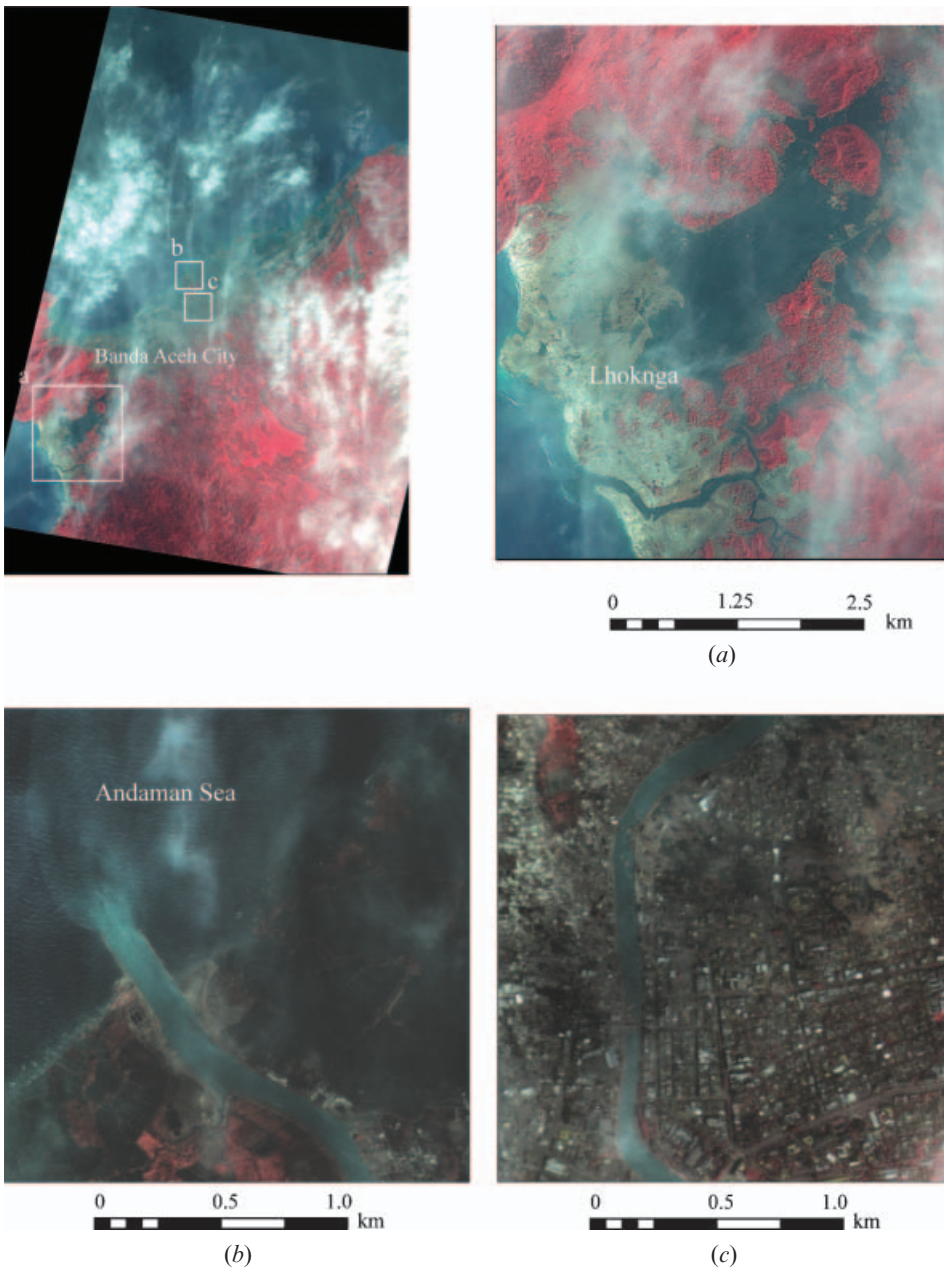(*e*1) (*e*2)

Figure 7. (*Continued.*)

Figure 8. Worst-hit region: Aceh province. (*a*) Struck and flooded Lhoknga. (*b*) Polluted water of one tributary of Aceh River with high suspended solids and wastes toward the Andaman Sea. (*c*) Badly destroyed traffic infrastructure and buildings in downtown Banda Aceh City.

tsunami. There are two clinics providing medical aid in Patong, in which Patong Merlin Clinic was struck by the tsunami in figure 7(*e*1) and Royal Paradise Clinic was safe to take care of the wounded in the catastrophe (figure 7(*e*2)).

Through haze reduction (using a 3×3 high-frequency kernel) and Gaussian contrast adjustment on the FORMOSAT-2 image of 28 December, the authorities
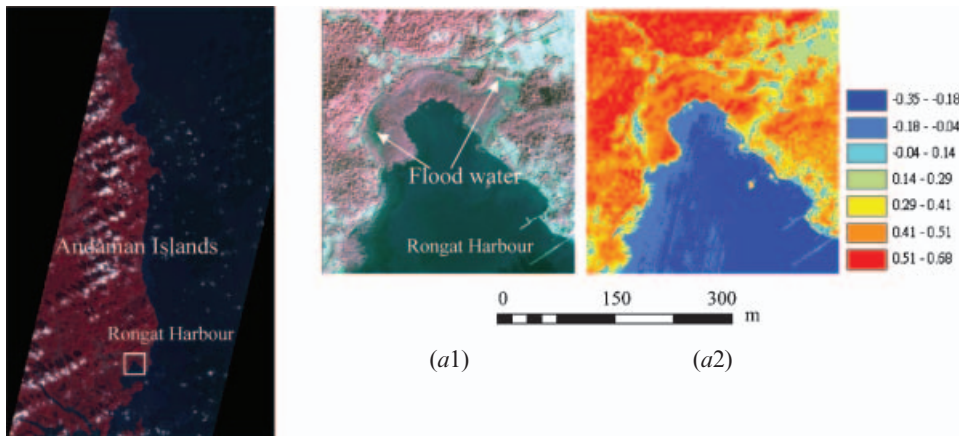
Figure 9. False-colour IR fusion image of the eastern Andaman Islands taken on 29 December 2004. (*a*1) Flood water still left on the land beside Rongat Harbour 3 days after the tsunami. (*a*2) NDVI analysis of the neighbourhood revealing a moderate change in vegetation cover after the tsunami.
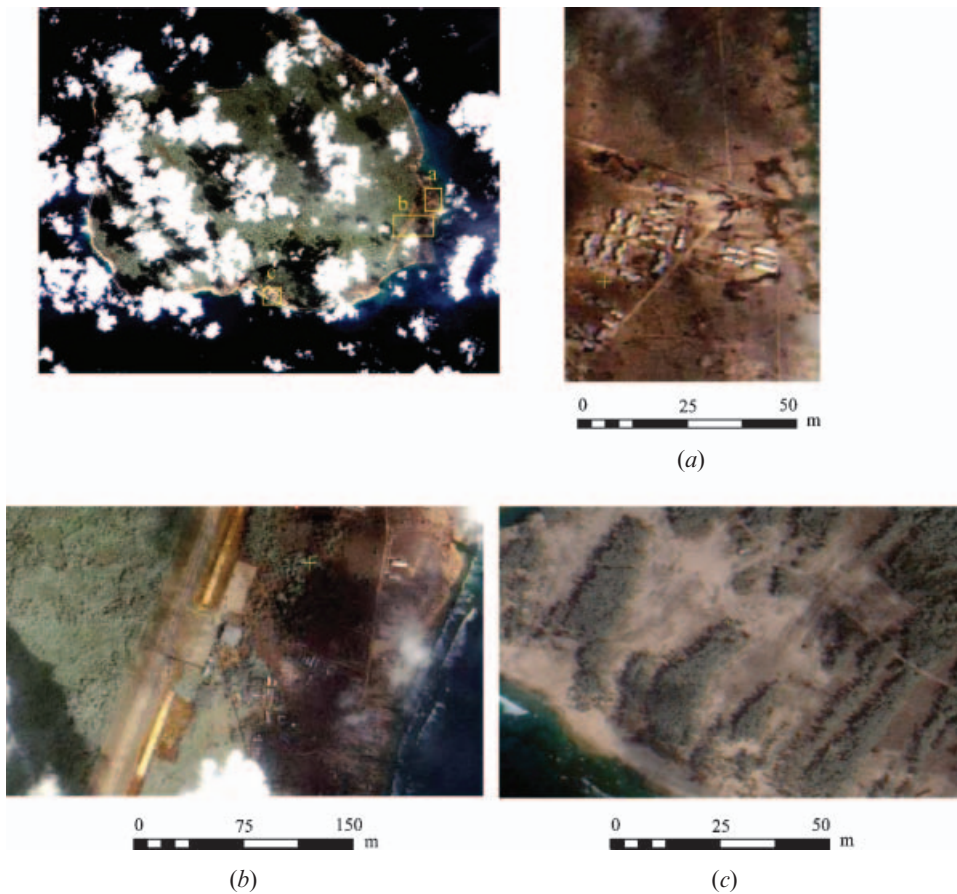

Figure 10. Fusion true-colour image of Car Nicobar, one of the Andaman Islands. (*a*) Struck village on Car Nicobar. (*b*) Devastated local airport by the tsunami. (*c*) North-east-trending scooping traces in southern Car Nicobar.
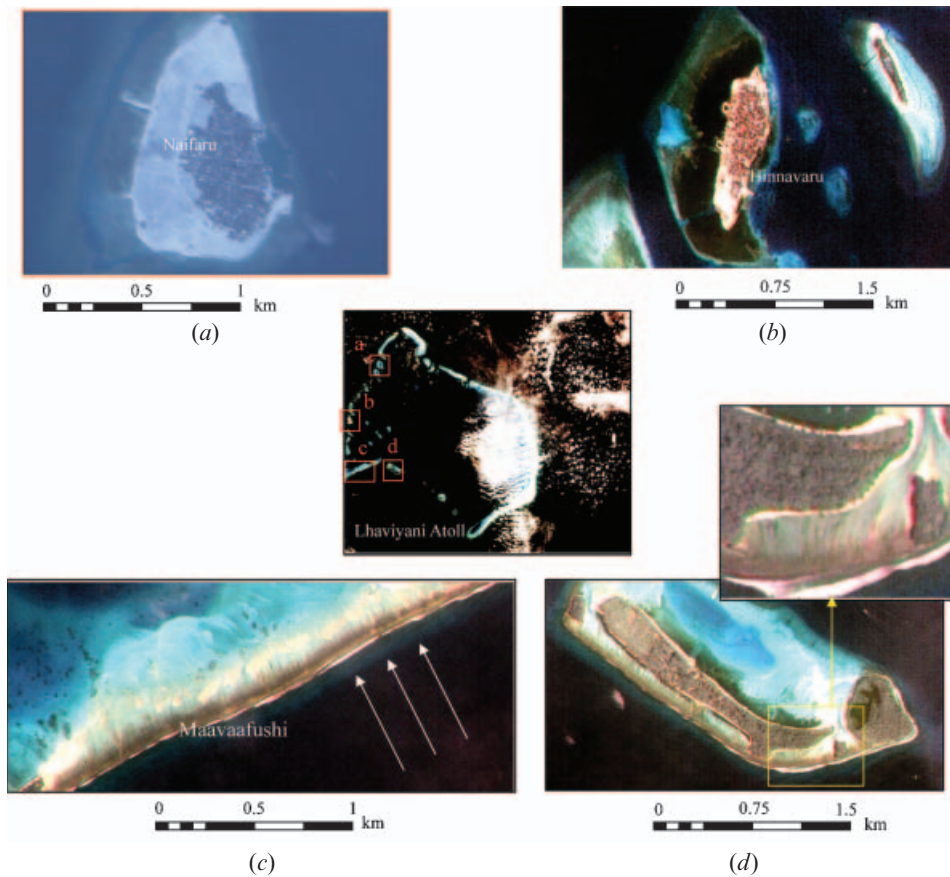
Figure 11.   Fusion true-color image of several main islands of the Maldives. (*a*) Mostly immersed Naifaru. (*b*) Several virtually wiped-out islands. (*c*) New born north-west-trending stripes along the coastline in Maavaafushi after the tsunami. (*d*) North–south-trending scouring in one island after the tsunami.

and public can gain a better glimpse of the devastated west coast of Indonesia's Sumatra Island, nearest the epicentre of the massive quake and tsunami. Many coastal areas of north-western Sumatra were badly hit by the massive quake-driven walls of water. Aceh province in particular suffered extensive damage and loss of life in this catastrophe. Figure 8(*a*) shows that Lhoknga area was severely struck and flooded by the tsunami. The tsunami swashed up to about 3–4 km inland and destroyed the forests and farmland in the coastal regions. More analyses of the tsunami effects in Banda Aceh, including inundation distance, shoreline erosion, and coseismic subsidence, can also be found in Borrero's investigation report (2005). Figure 8(*b*) shows that one of the Aceh River tributaries crossing downtown toward to the Andaman Sea was polluted by sea water, mud flow, and wastes. Thus, the invaded city was expected to be severely afflicted with problems of water resources and environmental pollution. Pure water shortage and overwhelmed aquatic ecosystems need to be focused on during the hazard recovery. Figure 8(*c*) is zoom-in subset showing the badly destroyed traffic infrastructures and buildings in downtown Banda Aceh City. The city was flooded and blanketed with mud and

rubble after the 9.0 magnitude quake and tsunami (which made the emergency rescue and recovery more difficult).

Figure 9 shows a false-colour NIR fusion image of the eastern Andaman Islands taken on 29 December 2004. Some flood water was still left on the land beside Rongat Harbour in figure 9(a1). In figure 9(a2), the NDVI values of the neighbourhood of Rongat Harbour remained quite constant pre- and post-tsunami, revealing that the vegetation cover was not severely destroyed by the tsunami probably because of the steep slope terrain. Figure 10(a) shows a fusion true-colour image of a struck village on Car Nicobar, one of the Andaman Islands. The tsunami brought by the flood wave covered most of the village, so after rescuing survivors, an intensive clean-up was the next task, to prevent secondary hazards from environmental pollution and diseases. Unfortunately, the local airport was also devastated by the tsunami, as shown in figure 10(b). The runway in the airfield was also covered by the tsunami, possibly resulting in transportation with the outside during the post-tsunami disaster response being cut off. In southern Car Nicobar, the scooping traces can be depicted by true-colour fusion imagery, as shown in figure 10(c), which indicates the attacking direction of the massive waves. Moreover, in addition to landslide, the vegetation in the coast region was seriously destroyed.

In one of the first visits to the battered islands, FORMOSAT-2 flew over islands in the Maldives, a famous holiday resort in the Indian Ocean. Figure 11 shows the true-colour fusion image of the main islands of the North Male' Atoll in the Maldives. Figure 11(a) shows that most of Naifaru was destroyed and immersed in the water. Several islands were virtually wiped out by the tsunami, as shown in figure 11(b). Figure 11(c) is a map of Maavaafushi, also named the 'Sunshine Coast'. Newly formed stripes along the coastline were left after the strike of the tsunami, which indicates the attacking direction of the tsunami shown by the white arrows. Similar scourings were found in other islands with the same attacking direction from the tsunami in figure 11(d).

6. Conclusions

Although satellite remote sensing has long been advocated for monitoring terrain changes, satellite images with a high temporal resolution indeed are an advancement in disaster monitoring. FORMOSAT-2 can efficiently contribute timely information for disaster response and recovery due to its high spatial and temporal resolutions. Especially for an instant response to a natural disaster, FORMOSAT-2 images can be acquired in 2 days at most through an emergency order. In this paper, the use of FORMOSAT-2 images of the severe Sumatra earthquake and tsunami demonstrated that it is a useful method of disaster monitoring. Through digital-image processes, some results of image analysis and interpretation were useful for instant response and rescue and are helpful for hazard recovery. The FORMOSAT-2 fusion images provide rich information necessary for hazard assessment and mitigation. FORMOSAT-2 imagery, especially fusion imagery, from 28 and 29 December 2004 clearly revealed the extension of flooding and widespread devastation to the coastal cities and surrounding areas. Evidently, the contribution of FORMOSAT-2 to provide the most up-to-date images available to hand can be appraised. However, the analysis and interpretation of images were limited due to the limited on-site information. More advanced image processes can be executed based on the acquisition of local geographic and environmental information to establish a sound and comprehensive recovery plan and distribution of indemnities for those disaster areas.

In addition to the contribution of the South Asia disaster, further developments in space science and technology for Taiwan NSPO will be aggressively searched for in research centres, universities, and technology institutes worldwide for conducting space-related research projects and cooperation. Thus, remote sensing has been playing a key role in disaster mitigation and damage assessment, and will become comprehensive in hazard management as more commercial remote-sensing satellites begin operations in the upcoming years.

Acknowledgements

References

BORRERO, J.C., 2005, Field data and satellite imagery of tsunami effects in Banda Aceh. *Science*, **308**, pp. 1596–1596.

CHANG, K.C., WU, F., CHEN, H., CHEN, C.K. and DUAN, C.R., 2004, Applying ROCSAT-2 image in 0702 hazard evaluation. In *The 23rd Conference of Surveying Theorem and Applications*, 9–10 September 2004, Taichung, Taiwan, V.J.D. Tsai, pp. 339–357 (Taichung, Taiwan: National Chung Hsing University) (in Chinese).

CHEN, C.M., HEPNER, G.F. and FORSTER, R.R., 2003, Fusion of hyperspectral and radar data using the HIS transformation to enhance urban surface features. *ISPRS Journal of Photogrammetry and Remote Sensing*, **58**, pp. 19–30.

CHEN, H., WU, F. and LIU, C., 2004, Introduction to ROCSAT-2 terminal. In *The 23rd Conference of Surveying Theorem and Applications*, 9–10 September 2004, Taichung, Taiwan, V.J.D. Tsai, pp. 333–338 (Taichung, Taiwan: National Chung Hsing University) (in Chinese).

CHEN, L., 2003, A study of applying genetic programming to reservoir Trophic state evaluation using remote sensor data. *International Journal of Remote Sensing*, **24**, pp. 2265–2275.

CHENG, K.S. and LEI, T.C., 2001, Reservoir Trophic state evaluation using Landsat TM images. *Journal of the American Water Resources Association*, **37**, pp. 1321–1334.

GANAS, A., AERTS, J., ASTARAS, T., VENTE, D., FROGOUDAKIS, E., LAMBRINOS, N., RISKAKIS, C., OIKONOMIDIS, D., FILIPPIDIS, A. and KASSOLI-FOURNARAKI, A., 2004, The use of Earth observation and decision support systems in the restoration of open-cast nickel mines in Evia, central Greece. *International Journal of Remote Sensing*, **25**, pp. 3261–3274.

GANAS, A., PAPADOPOULOS, G. and PAVLIDES, S.B., 2001, The 7 September 1999 Athens 5.9 Ms earthquake: remote sensing and digital elevation model inputs towards identifying the seismic fault. *International Journal of Remote Sensing*, **22**, pp. 191–196.

GUPTA, B.P. and JOSHI, B.C., 1990, Landslide hazard zoning using the GIS approach – a case study from Ramganga Catchment, Himalayas. *Engineering Geology*, **28**, pp. 119–131.

KOGAN, F.N., 1997, Global drought watch from space. *Bulletin of the American Metrological Society*, **78**, pp. 621–636.

LIN, C.W., LIU, C.C., LEE, S.Y., TSANG, Y.C., LIE, S.H., CHIU, Y.C., WU, A.M., WU, F.F. and CHEN, H.Y., 2004b, Assessment of the typhoon Mindulle induced hazard using ROCSAT-2 imagery—Chenyulan River and Tachia River watershed. In *The 23rd conference of Surveying theorem and applications*, 9–10 September 2004, Taichung, Taiwan, edited by V.J.D. Tsai. Department of Civil Engineering, National Chung Hsing University, Taichung, Taiwan, pp. 367–378 (in Chinese).

LIN, C.Y., LO, H.M., CHOU, W.C. and LIN, W.T., 2004a, Vegetation recovery assessment at the Jou-Jou Mountain landslide area caused by the 921 Earthquake in Central Taiwan. *Ecological Modelling*, **179**, pp. 75–81.

LIN, P.S., HUNG, J.C., LIN, J.Y. and YANG, M.D., 2000, *Risk assessment of potential debris-flows using GIS, Debris-Flow Hazards Mitigation: Mechanics, Prediction, and Assessment* (Rotterdam: Balkema), 608.

LIN, P.S., LIN, J.Y., HUNG, J.C. and YANG, M.D., 2002, Assessing debris-flow hazard in a watershed in Taiwan. *Engineering Geology*, **66**, pp. 295–313.

MONTOYA, L., 2003, Geo-data acquisition through mobile GIS and digital video: an urban disaster management perspective. *Environmental Modelling and Software*, **18**, pp. 869–876.

MURTHY, C.S., RAJU, P.V. and BADRINATH, K.V.S., 2003, Classification of wheat crop with multi-temporal images: performance of maximum likelihood and artificial neural networks. *International Journal of Remote Sensing*, **24**, pp. 4871–4890.

NSPO, 2005, Available online at: http://www.nspo.org.tw/e60/menu0401.html (accessed 21 July 2005).

PIWOWAR, J.M., PDEELE, D.R. and LEDREW, E.F., 1998, Temporal mixture analysis of Arttic sea ice imagery: a new approach for monitoring environmental change. *Remote Sensing of Environment*, **63**, pp. 195–207.

RIVEREAU, J.C., 1995, Spot data applied to disaster prevention and damage assessment. *Acta Astronautica*, **35**, pp. 467–470.

RYDBERG, A. and BORGEFORS, G., 2001, Integrated method for boundary delineation of agricultural fields in multispectral satellite images. *IEEE International Geoscience and Remote Sensing*, **39**, pp. 2514–2520.

TRALLI, D.M., BLOM, R.G., ZLOTNICKI, V., DONNELLAN, A. and EVANS, D.L., 2005, Satellite remote sensing of earthquake, volcano, flood, landslide and coastal inundation hazards. *ISPRS Journal of Photogrammetry and Remote Sensing*, **59**, pp. 185–198.

TRAMUTOLI, V., CUOMO, V., FILIZZOLA, C., PERGOLA, N. and PIETRAPERTOSA, C., 2005, Assessing the potential of thermal infrared satellite surveys for monitoring seismically active areas: The case of Kocaeli (Izmit) earthquake, August 17, 1999. *Remote Sensing of Environment*, **96**, pp. 409–426.

USGS, 2005, Available online at: http://earthquake.usgs.gov/eqinthenews/2004/usslav (accessed 21 July 2005).

VAN DER SANDE C.J., DEJONG, S.M. and DEROO, A.P.J., 2003, A segmentation and classification approach of IKONOS-2 imagery for land cover mapping to assist flood risk and flood damage assessment. *International Journal of Applied Earth Observation*, **4**, pp. 217–229.

VIGNY, C., SIMONS, W.J.F., ABU, S., BAMPHENYU, R., SATIRAPOD, C., CHOOSAKUL, N., SUBARYA, C., SOCQUET, A., OMAR, K., ABIDIN, H.Z. and AMBROSIUS, B.A.C., 2005, Insight into the 2004 Sumatra-Andaman earthquake from GPS measurements in southeast Asia. *Nature*, **436**, pp. 201–206.

WU, A.M. and WU, F., 2004, Applications of ROCSAT-2 images. In *The 23rd Conference of Surveying Theorem and Applications*, 9–10 September 2004, Taichung, Taiwan, V.J.D. Tsai, pp. 359–366 (Taichung, Taiwan: National Chung Hsing University) (in Chinese).

YA'ALLAH S.M. and SARADJIAN, M.R., 2005, Automatic normalization of satellite images using unchanged pixels within urban areas. *Information Fusion*, **6**, pp. 235–241.

YANG, M.D., MERRY, C.J. and SYKES, R.M., 1999, Integration of water quality modeling, remote sensing, and GIS. *Journal of American Water Resources Association*, **35**, pp. 253–263.

YANG, M.D., HSU, C.H. and SU, D.C., 2005, DBI and SI as fitness in GA classification for remote sensing imagery. In *2005 IEEE International Geoscience and Remote Sensing Symposium*, Seoul, pp. 3741–3744.

YANG, M.D. and YANG, Y.F., 2004, Genetic algorithm for unsupervised classification of remote sensing imagery. In Image Processing: Algorithms and Systems III, edited by E.R. Dougherty, J.T. Astola, and K.O. Egiazarian. *Proceedings of SPIE-IS&T and Electronic Imaging, SPIE*, **5298**, pp. 395–402.

YANG, M.D., YANG, Y.F. and HSU, S.C., 2004, Application of remotely sensed data to the assessment of terrain factors affecting Tsao-Ling landside. *Canadian Journal of Remote Sensing*, **30**, pp. 593–603.

YANG, X.Y. and LO, C.P., 2000, Relative radiometric normalization performance for change detection from multi-date satellite images. *Photogrammetric Engineering and Remote Sensing*, **66**, pp. 967–980.